Article:
Alahmadi, Y.H., Awadh, S.A. and Nowakowski, A.F. (2021) Simulation of swirling flow with a vortex breakdown using modified shear stress transport model. Industrial and Engineering Chemistry Research, 60 (16). pp. 6016-6020. ISSN: 0888-5885

https://doi.org/10.1021/acs.iecr.1c00158

I&EC research
Industrial & Engineering Chemistry Research
pubs.acs.org/IECR
Article

Simulation of Swirling Flow with a Vortex Breakdown Using Modified Shear Stress Transport Model

Yaser H. Alahmadi, Sawsan A. Awadh, and Andrzej F. Nowakowski*

Cite This: *Ind. Eng. Chem. Res.* 2021, 60, 6016−6026

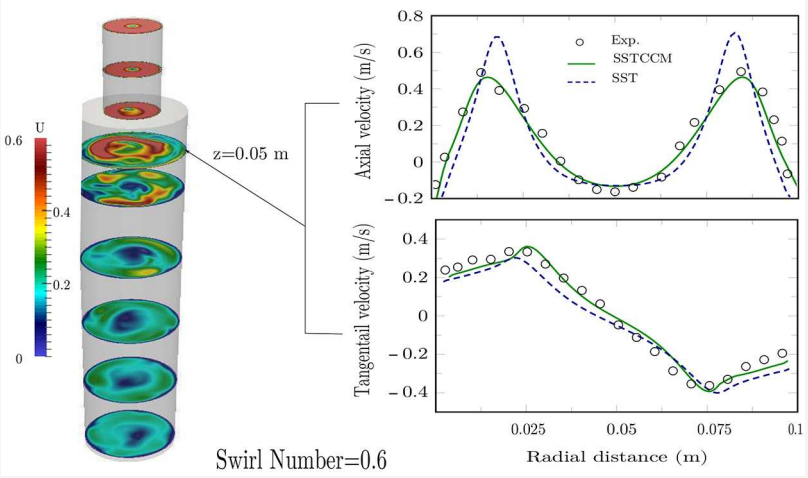

ABSTRACT: The well-known Shear Stress Transport (SST $k-\omega$) turbulence model was modified and examined. Two industrially relevant problems with curved and rotating channels have been selected to assess the modification potential: a rotating lid in a confined cylinder and swirling flow through a three-dimensional abrupt expansion pipe. The postulated amendment simplified the rotation and curvature correction term that was suggested earlier by Smirnov and Menter [*J. Turbomach.* **2009**, *131* (4) 041010]. The new formulation avoids the calculation of the complex Lagrangian derivatives by implementing the Richardson number (Ri) in the applied rotation function. The numerical computations were performed using OpenFOAM-2.4.x. The results show the expected capability of the Shear Stress Transport model with Curvature Correction Modification (SSTCCM) to handle the curvature effects and system rotation. The paper compares the SSTCCM model with the conventional eddy viscosity models (EVMs): standard $k-\epsilon$; Re-Normalization Group (RNG) $k-\epsilon$, and the original SST $k-\omega$.

INTRODUCTION

One of the most remarkable drawbacks of the eddy viscosity models (EVMs) is their inability to capture the flow behavior in a rotating system and streamline curvature. For example, for complex cases of fluidic devices without moving parts where the flow demonstrates a high level of rotational motion, EVMs fail to predict these effects accurately. The main reason for this deficiency is due to the use of the Boussinesq hypothesis, which assumes the eddy viscosity as an isotropic scalar, which is incorrect for complex flows with a rotating system. Since 1980, various attempts of modifications and improvements on different EVMs have been proposed to enhance these models (see refs 1−3). However, these models are still inadequate to address three-dimensional (3D) flows. Later, in 1997, Spalart and Shur[4] proposed an empirical approach on the sensitization of the Spalart−Allmaras turbulence model to rotation and curvature effects. This model demonstrated its valuable ability to capture a high level of turbulence. Unlike the approach proposed by Knight and Saffman,[5] Spalart and Shur's model is more efficient, because it measures the extra influence of the invariant contributor to the turbulence. By 2009, Smirnov and Menter[6] had adapted the rotation−curvature correction function proposed earlier in Spalart and Shur[4] to the shear stress transport $k-\omega$ model (SST $k-\omega$). The correction function was applied to the production term in both the k and ω transport equations. As a result, the corrected model, denoted as the SSTCC, is more accurate, computationally efficient, and robust than its predecessor.

Received: January 12, 2021
Revised: March 19, 2021
Accepted: April 6, 2021
Published: April 15, 2021

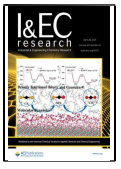

https://doi.org/10.1021/acs.iecr.1c00158
Ind. Eng. Chem. Res. 2021, 60, 6016−6026

In this work, the Richardson number (Ri) has been implemented to avoid the need to calculate the Lagrangian derivatives term (DS_{ij}/Dt), which appears in the nondimensional argument $\tilde{r}$. This leads to a simpler version of the SSTCC, which is realized by implementing the Ri number. As a result, the obtained numerical code requires lower computational cost and is also competitive, in terms of accuracy, when compared to the conventional EVMs. The new formula for $\tilde{r}$ is applied into the rotation function developed in Smirnov and Menter.[6] The initial attempt to investigate the performance and accuracy of the developed SSTCCM model has been discussed in the report by Alahmadi and Nowakowski.[7] The work of Alahmadi and Nowakowski was predominantly focused on a specific case of cyclone operation and therefore was restricted, with regard to thorough analyses of the model. The objective of this contribution is to investigate the performance of the SSTCCM model in a range of different physical scenarios that include a vortex breakdown and to compare it with other available models.

This paper is organized as follows. The formulation of the proposed SSTCCM model is presented first. Then, it is applied to the simulation of two cases: (1) a rotating lid in a confined cylinder and (2) turbulent swirling flow through an abrupt expansion. For each test case, a description of the problem, numerical methods, and the simulation results are presented and discussed in details. Finally, major findings and conclusions of the paper are summarized.

MODEL FORMULATION

The Navier−Stokes equations describe the physics of fluid motion. The continuity and momentum equation respectively represent the mass conservation equation and incompressible form of Navier−Stokes equations as follows:

$$\frac{\partial u_i}{\partial x_i} = 0 \tag{1}$$

$$\rho\frac{\partial u_i}{\partial t} + \rho\frac{\partial u_i u_j}{\partial x_j} = -\frac{\partial p}{\partial x_i} + \frac{\partial}{\partial x_j}(2\mu s_{ij}) \tag{2}$$

where u and p represent the velocity and pressure. The term s_{ij} is the strain-rate tensor, which is written as

$$s_{ij} = \frac{1}{2}\left(\frac{\partial u_i}{\partial x_j} + \frac{\partial u_j}{\partial x_i}\right) \tag{3}$$

The flow variables in eqs 1 and 2 are decomposed into mean and fluctuating quantities. The time average process then is applied, which yields the final form of the Reynolds-averaged Navier−Stokes equations, which can be written as follows:

$$\frac{\partial \overline{u_i}}{\partial x_i} = 0 \tag{4}$$

$$\rho\frac{\partial \overline{u_i}}{\partial t} + \rho\frac{\partial \overline{u_i u_j}}{\partial x_j} = -\frac{\partial \overline{p}}{\partial x_i} + \frac{\partial}{\partial x_j}(2\mu S_{ij} - \rho\overline{u_i' u_j'}) \tag{5}$$

The term S_{ij} is the time-averaged quantity of the strain-rate tensor. The appearance of the additional term τ_{ij} (which is defined as $\tau_{ij} = -\rho\overline{u_i' u_j'}$) is known as the Reynolds stress tensor. In order to find a solution to the mathematical problem, the system of equations must be closed by evaluating a specific term of τ_{ij}. This is the main principle that must be followed when designing any turbulence model.

Menter SST Turbulence Model. In 1994, Menter[8] introduced the shear stress transport (SST) model, which is an improved version of the two-equation $k-\omega$ model. The SST model combines the two turbulence models ($k-\omega$ and $k-\epsilon$). The $k-\omega$ model is used in the inner part of the boundary layer and switches to the $k-\epsilon$ model in the free streamflow. The SST model employs the Boussinesq hypothesis to relate the Reynolds stresses to the mean rate of deformation as follows:

$$\tau_{ij} = -\rho\overline{u_i' u_j'} = \mu_t\left(2S_{ij} - \frac{2}{3}\frac{\partial u_k}{\partial x_k}\delta_{ij}\right) - \frac{2}{3}\rho k\delta_{ij} \tag{6}$$

The conservation form of the transport equations for both the turbulence kinetic energy (k) and the turbulent frequency (ω) can be written as

$$\rho\frac{\partial(k)}{\partial t} + \rho\frac{\partial(u_j k)}{\partial x_j} = P_k - \beta^*\rho k\omega + \frac{\partial}{\partial x_j}\left[(\mu + \sigma_k\mu_t)\frac{\partial k}{\partial x_j}\right] \tag{7}$$

$$\rho\frac{\partial(\omega)}{\partial t} + \rho\frac{\partial(u_j\omega)}{\partial x_j} = P_k\frac{\rho}{\mu_t} - \beta\rho\omega^2 + \frac{\partial}{\partial x_j}\left[(\mu + \sigma_\omega\mu_t)\frac{\partial\omega}{\partial x_j}\right] + 2(1 - F_1)\frac{\rho\sigma_{\omega 2}}{\omega}\frac{\partial k}{\partial x_j}\frac{\partial\omega}{\partial x_j} \tag{8}$$

The production term P_k is defined as

$$P_k = \tau_{ij}\frac{\partial u_i}{\partial x_j} = \left[\mu_t\left(2S_{ij} - \frac{2}{3}\frac{\partial u_k}{\partial x_k}\delta_{ij}\right) - \frac{2}{3}\rho k\delta_{ij}\right]\frac{\partial u_i}{\partial x_j} \tag{9}$$

where the turbulent viscosity is defined as follows:

$$\mu_t = \frac{\rho a_1 k}{\max(a_1\omega, \Omega F_2)} \tag{10}$$

The blinding function F_1 in the free stream is zero ($k-\epsilon$ model) and, in the boundary layer, is equal to one ($k-\omega$ model), given by

$$F_1 = \tanh(\arg_1{}^4) \tag{11}$$

$$\arg_1 = \min\left[\max\left(\frac{\sqrt{k}}{\beta^*\omega d}, \frac{500\nu}{d^2\omega}\right), \frac{4\rho\sigma_{\omega 2}k}{CD_{k\omega}d^2}\right] \tag{12}$$

$$CD_{k\omega} = \max\left(2\rho\sigma_{\omega 2}\frac{1}{\omega}\frac{\partial k}{\partial x_j}\frac{\partial\omega}{\partial x_j}, 10^{-20}\right) \tag{13}$$

$$F_2 = \tanh(\arg_2{}^2) \tag{14}$$

$$\arg_2 = \max\left(2\frac{\sqrt{k}}{\beta^*\omega d}, \frac{500\nu}{d^2\omega}\right) \tag{15}$$

The constant closure coefficients of the SST model are given in Table 1.

Spalart−Allmaras Rotation Curvature (SARC) Turbulence Model. The standard Spalart−Allmaras (SA) turbulence model does not account for the effects of system rotation and streamline curvature. Spalart and Shur[4] proposed an empirical alteration to the original standard SA model. As a result, the production term of turbulence viscosity equation is multiplied by a rotation function f_{r1}, which is given by

https://doi.org/10.1021/acs.iecr.1c00158
Ind. Eng. Chem. Res. 2021, 60, 6016−6026

Table 1. SST $k-\omega$ Closure Constants

closure coefficient	value
κ	0.4187
σ_k	0.85
σ_ω	0.5
$\sigma_{\omega 2}$	0.856
β_1	0.0785
β_2	0.0828
β^*	0.09
a_1	0.31

$$f_{r1}(r^*, \tilde{r}) = (1 + c_{r1})\frac{2r^*}{1 + r^*}[1 - c_{r3}\tan^{-1}(c_{r2}\tilde{r})] - c_{r1} \tag{16}$$

The formula contains the dimensionless quantities r^* and $\tilde{r}$, which are defined as

$$r^* = \frac{S}{\Omega} \tag{17}$$

and

$$\tilde{r} = \frac{2\omega_{ik}S_{jk}}{D^4}\left[\frac{DS_{ij}}{Dt} + (\varepsilon_{imn}S_{jn} + \varepsilon_{jmn}S_{in})\Omega_m\right] \tag{18}$$

The term DS_{ij}/Dt in eq 18 represents the components of the Lagrangian derivatives of the strain tensor, and ε_{imn} is the Levi–Civita symbol. The empirical constants c_{r1}, c_{r2}, and c_{r3} that appear in eq 16 are given the values 1.0, 2.0, and 1.0, respectively.

The function (f_{r1}) enhances the performance of the SA model.[9] However, it is rather complex and increases the computational cost. This is due to the factor accounting for the rotation-curvature correction that contains Lagrangian derivative DS_{ij}/Dt and a higher-order derivative of the strain-rate tensor term D^4 in eq 18.

SSTCCM Model. The model presented in this paper builds on the shear stress transport model (SST $k-\omega$) and also on the rotation function that was proposed in the work of Smirnov and Menter.[6] The Richardson number Ri, which was defined by Hellsten,[10] is used to avoid calculating the terms D^4 and the complex Lagrangian derivatives in eq 18. To control the production term P_k that appears in the transport equations, the modified rotation function is used. The incompressible form of the transport equations of the turbulent kinetic energy and its specific dissipation for the SSTCCM model can be cast in differential form:

$$\rho\frac{\partial(k)}{\partial t} + \rho\frac{\partial(u_j k)}{\partial x_j} = f_{rot}P_k - \beta^*\rho k\omega + \frac{\partial}{\partial x_j}\left[(\mu + \sigma_k\mu_t)\frac{\partial k}{\partial x_j}\right] \tag{19}$$

$$\rho\frac{\partial(\omega)}{\partial t} + \rho\frac{\partial(u_j\omega)}{\partial x_j} = f_{rot}P_k\frac{\rho}{\mu_t} - \beta\rho\omega^2 + \frac{\partial}{\partial x_j}\left[(\mu + \sigma_\omega\mu_t)\frac{\partial\omega}{\partial x_j}\right] + 2(1 - F_1)\frac{\rho\sigma_{\omega 2}}{\omega}\frac{\partial k}{\partial x_j}\frac{\partial\omega}{\partial x_j} \tag{20}$$

The production term P_k and the blinding function F_1 are given in eqs 9 and 11, respectively. The rotation function (f_{rot}) is defined as

$$f_{rot} = \max\{\min(f_{r1}, 1.25), 0.0\} \tag{21}$$

The term f_{r1} is the rotation function presented in eq 16 and has been defined by Spalart and Shur.[4] The production term that appears in the SA model is based on the vorticity tensor (Ω), which characterizes the rotation, while the production term P_k is based on the strain-tensor rate S, which characterizes the total deformation. Therefore, P_k is greater than $\tilde{S}$, which justifies the use of the limiter in the rotating function f_{rot}.[6] The dimensionless quantities $\tilde{r}$, which exactly represents the Richardson number Ri, as defined by Hellsten,[10] and r^* are then given as follows:

$$\tilde{r} = \frac{\Omega}{S}\left(\frac{\Omega}{S} - 1\right)r^* = \frac{S}{\Omega} \tag{22}$$

The Ri term includes the effects of rotation and the significance of the streamline curvature effect by accounting for the mean flow deformation. The direct reference to Ri avoids computing thre Lagrangian derivative DS_{ij}/Dt and a higher-order derivative of the strain-rate tensor term D^4 in eq 18. Here, the strain-tensor rate S and the vorticity tensor Ω represent the following expressions:

$$S = (2S_{ij}S_{ij})^{1/2} \quad \text{and} \quad \Omega = (2\omega_{ij}\omega_{ij})^{1/2} \tag{23}$$

where

$$S_{ij} = \frac{1}{2}\left(\frac{\partial u_i}{\partial x_j} + \frac{\partial u_j}{\partial x_i}\right)$$

$$\omega_{ij} = \left[2\varepsilon_{mji}\Omega_m + \frac{1}{2}\left(\frac{\partial u_i}{\partial x_j} - \frac{\partial u_j}{\partial x_i}\right)\right]$$

$$D^2 = \frac{1}{2}(S^2 + \Omega^2) \tag{24}$$

Numerical Implementation and Simulation Results. The described model has been implemented using the open source code OpenFOAM-2.4.x with flexible and extendable C++ libraries.[11] Finite volume grids have been used to calculate the results for all near-wall flows, resolving the viscous sublayer with $y^+ < 1$. To avoid any grid resolution uncertainties, highly refined grids have been created for all two-dimensional (2D) and three-dimensional (3D) simulations. The model was first tested for a confined cylinder with a rotating lid and verified with respect to experimental data using different numerical schemes. After that, the 3D swirling flow through a sudden expansion pipe was examined using the proposed model and compared with the classical SST model[8] and various conventional EVMs.

Rotating Lid in a Confined Cylinder. *Case Geometry and Numerical Settings.* The first test case that was chosen to validate the proposed model and compared to experimental data is a confined cylinder with a rotating lid, which has been studied by Fujimura et al.[12] This case constituted a criterion for the choice of the discretization scheme for the momentum equation convective term. The computational domain is shown in Figure 1a, which can be described as a confined cylinder, where the swirling flow is generated by a rotating lid at the top end-wall of the pipe. Because of the shear forces, the flow in contact with the rotating lid acquires a spinning motion. Consequently, the fluid particles are propelled radially outward, while near the sidewall, the fluid spirals down. As it reaches the bottom end-wall, the fluid reverses its direction and moves from the sidewall toward the central axis before spiraling upward.

https://doi.org/10.1021/acs.iecr.1c00158
Ind. Eng. Chem. Res. 2021, 60, 6016–6026

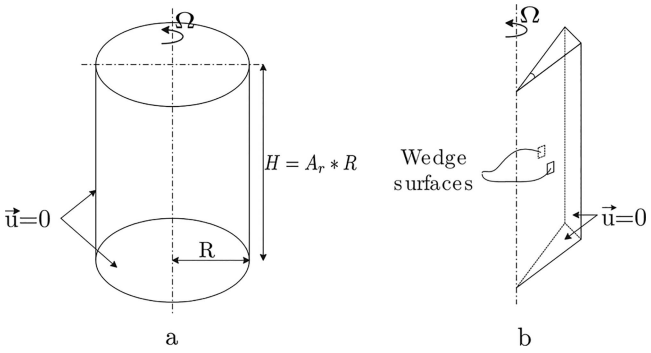

Figure 1. (a) Diagram of a confined cylinder with a rotating upper lid, showing the dimensions and the boundaries. (b) Axisymmetric 2D configuration.

The characteristics of the flow pattern of this swirling motion are mainly dependent on two dimensionless parameters, i.e., the Reynolds number Re (which is defined as $Re = R^2\Omega/\nu$) and the cylinder aspect ratio Ar (which is defined as $\mathrm{Ar} = H/R$), where R is the radius of the cylinder, Ω is the angular velocity of the lid, and H is the height of the cylinder. An axisymmetric 2D simulation is performed in order to facilitate the computational effort. The 2D axisymmetric computational domain is shown in Figure 1b. The numerical results are presented for aspect ratios of 1.5 and 2.5 with the corresponding Re values of 1010, 1290, and 2200, respectively. The relevant meshes are presented in

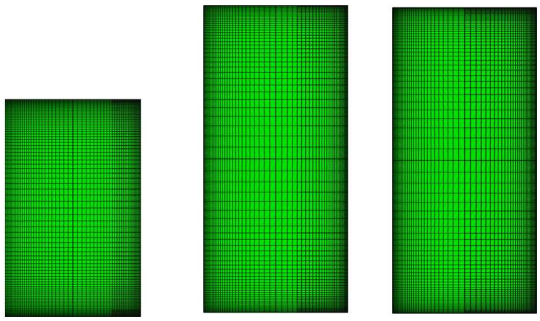

Figure 2. Fine-structured hexahedral mesh with y^+ less than unity. From left to right: case A, case B, and case C.

Figure 2. The mesh is refined according to the Re value with a y^+ value less than unity for all cases:

$$y^+ = Re\left(\frac{\Delta y_1 u_\tau}{R^2\Omega}\right) \tag{25}$$

where Δy_1 is the height of the first cell adjacent to the wall and u_τ is the frictional velocity.

The relationship between the parameters (Re and Ar) and vortex breakdown observations were reported by Escudier.[13] In this case study, three different regimes are considered. These area, which have been labeled Cases A, B, and C, correspond to the following values: Re = 1290 and Ar = 1.5, Re = 2200 and Ar = 2.5, and Re = 1010 and Ar = 2.5, respectively. The equations of the turbulence quantity variables (k and ω) are both discretized using the second-order linear upwind scheme (LU). The equations residuals for the investigated first- and second-order schemes were set to fall below a predetermined residual tolerance value over a successive number of iterations. For the pressure equation, the residual value was 10^{-8}, whereas, for all other variables, a value of 10^{-6} was considered sufficient.

RESULTS AND DISCUSSION

Figure 3 shows that the upwind scheme provides an erroneous streamlines for cases A and B. On the other hand, the second-order schemes (Self Filtered Central Differencing Scheme (SFCD) and LU) are both qualitatively in good agreement with the experimental measurements. Unlike the upwind scheme, the location and the number of the vortex breakdowns are accurately predicted by the second-order schemes.

Figure 4 shows that the SSTCCM model provides good predictions of the axial velocity profile along the longitudinal centerline, when compared to experimental data. In terms of accuracy and reliability, the second-order schemes are superior to the simple first-order scheme. For example, Table 2 shows that the upwind scheme for the fine mesh underestimates the maximum velocity by ∼10% for case A and by <1% for cases B and C. Although the upwind scheme seems to provide accurate predictions of the velocity profile, it cannot capture the formation of the vortex breakdown, as shown in Figure 3. The results of the second-order schemes demonstrate that the SFCD scheme provides insignificant improvement, in terms of the grid refinement. In contrast, the accuracy of the LU scheme is closely related to the grid refinement (see Tables 3 and 4). Therefore, the second-order LU scheme will be adopted for the sudden expansion case.

The 3D computations should resolve other flow features as geometry induces more intricate dynamics and the flow field is influenced by the stretching of vortical structures. The mechanism of vortex stretching is absent in 2D flows; therefore, the results could be qualitatively different from 3D results. There are also restrictions related to k–ω turbulence models. Simpson and Ranade[14] highlighted excessive predictions of turbulence kinetic energy in the vicinity of stagnation points, as well as the differences between 2D axisymmetric models and fully 3D approaches.

Swirling Flow through a 3D Sudden Expansion Pipe. Turbulent swirling flow through a 3D abrupt expansion can be found in various fluidic devices without moving parts. Examples are hydrocyclones,[15−17] cyclone separators,[18] jet ejectors,[19] or spray dryers.[20] The flow field is complex. It includes various dynamic phenomena that are manifested by extremely high levels of turbulence, recirculation, separation and reattachment as well as vortex breakdown. The initiation and determination of the location of the vortex breakdown and the flow instabilities can be construed because of the diverging nature of the expansion flow. Therefore, in order to predict this flow behavior correctly, particular attention must be paid to the choice of the turbulence closure. Despite of the numerous studies that have investigated vortex breakdown through the sudden expansion pipe, including refs 21−25, this type of flow is still not fully understood, particularly for high swirling flow with swirl numbers near unity.

The present work evaluates the capability of the new formulation by comparing its performance with different EVMs: standard k–ϵ; RNG k–ϵ, and SST k–ω. It then validates the results, using the experimental measurements of Dellenback et al.[21]

Case Geometry and Numerical Settings. The numerical configuration was based on the experiment of Dellenback et al.[21] The experiment was designed to investigate the turbulent swirling flow through an abrupt expansion with an aspect ratio of

https://doi.org/10.1021/acs.iecr.1c00158
Ind. Eng. Chem. Res. 2021, 60, 6016−6026

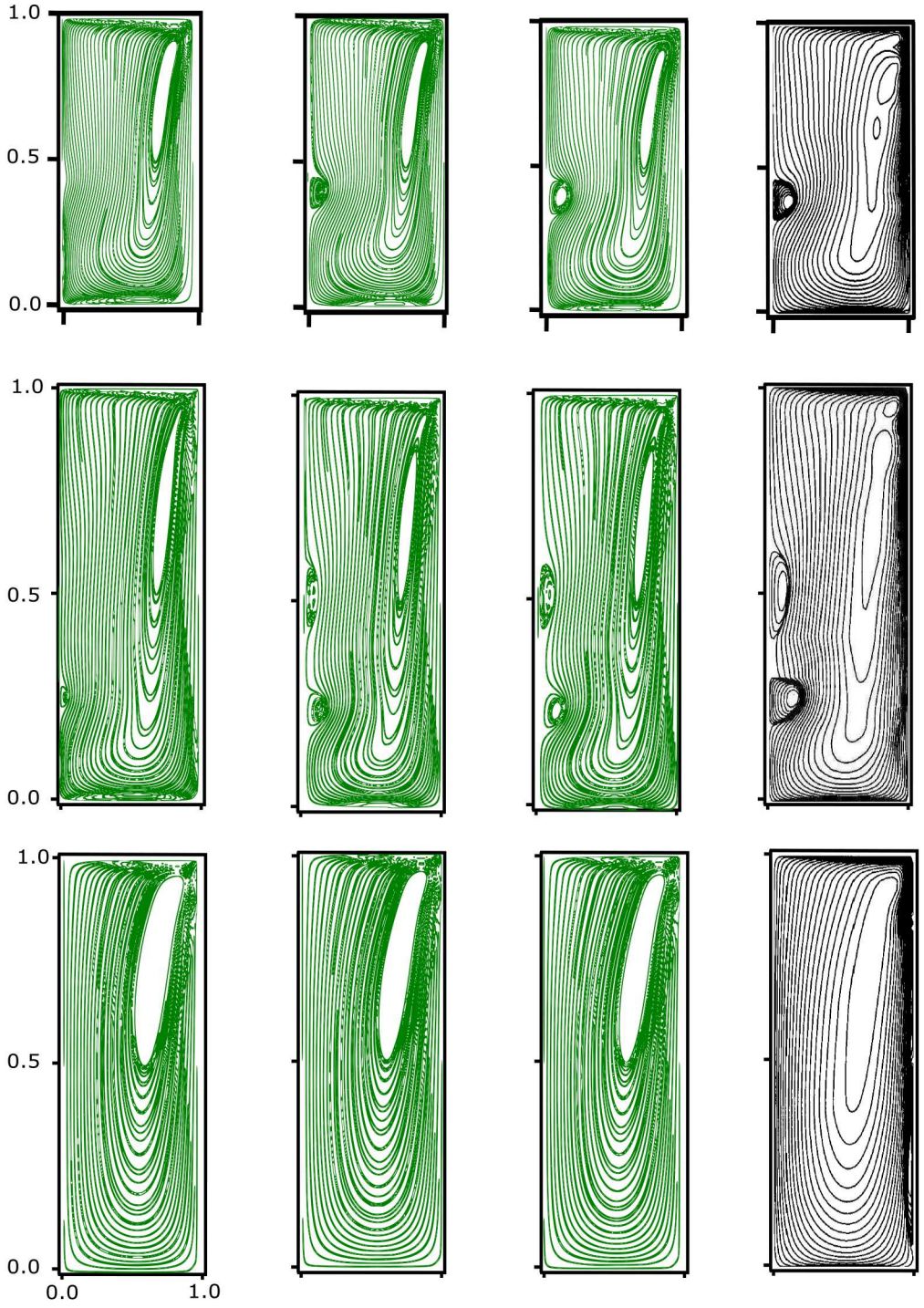

Figure 3. Contour plot of the streamlines, from top to bottom, Case A (Re = 1290, Ar = 1.5), Case B (Re = 2200, Ar = 2.5), and Case C (Re = 1010, Ar = 2.5); from left to right, upwind, SFCD, LU, and experimental visualizations. [Experimental results reprinted with permission from ref 12. Copyright 2001, American Society for Mechanical Engineers.]

1:1.94, using the laser Doppler anemometer LDA method. Figure 5 and Table 5 depict the computational domains used in the present study. The structured grid consists of hexahedral elements. A high-resolution discretization is applied close to the wall with a y^+ value of less than unity. The simulation was performed first on a course mesh, then on refined mesh that was obtained by doubling the number of grid points in each direction. This resulted in a negligible difference for all of the primitive variables. The final mesh that was implemented, which is depicted in Figure 6, consisted of 1 567 954 cells.

The Reynolds number, based on the upstream diameter D, is $Re = 3 \times 10^4$. The inlet section of the flow is placed at $x = -2D$, and an axisymmetric sudden expansion downstream is encountered at $x = 0$. Two cases for the inlet velocity has been set: either a pure axial velocity of (0.473), as stated in Table 6, or a swirling inlet boundary condition that is adjusted as an axisymmetric profile. The axial and tangential components of the inlet velocity profile are adapted from the experimental work of Dellenback et al.,[21] while the radial velocity is set to zero. The

https://doi.org/10.1021/acs.iecr.1c00158
Ind. Eng. Chem. Res. 2021, 60, 6016−6026

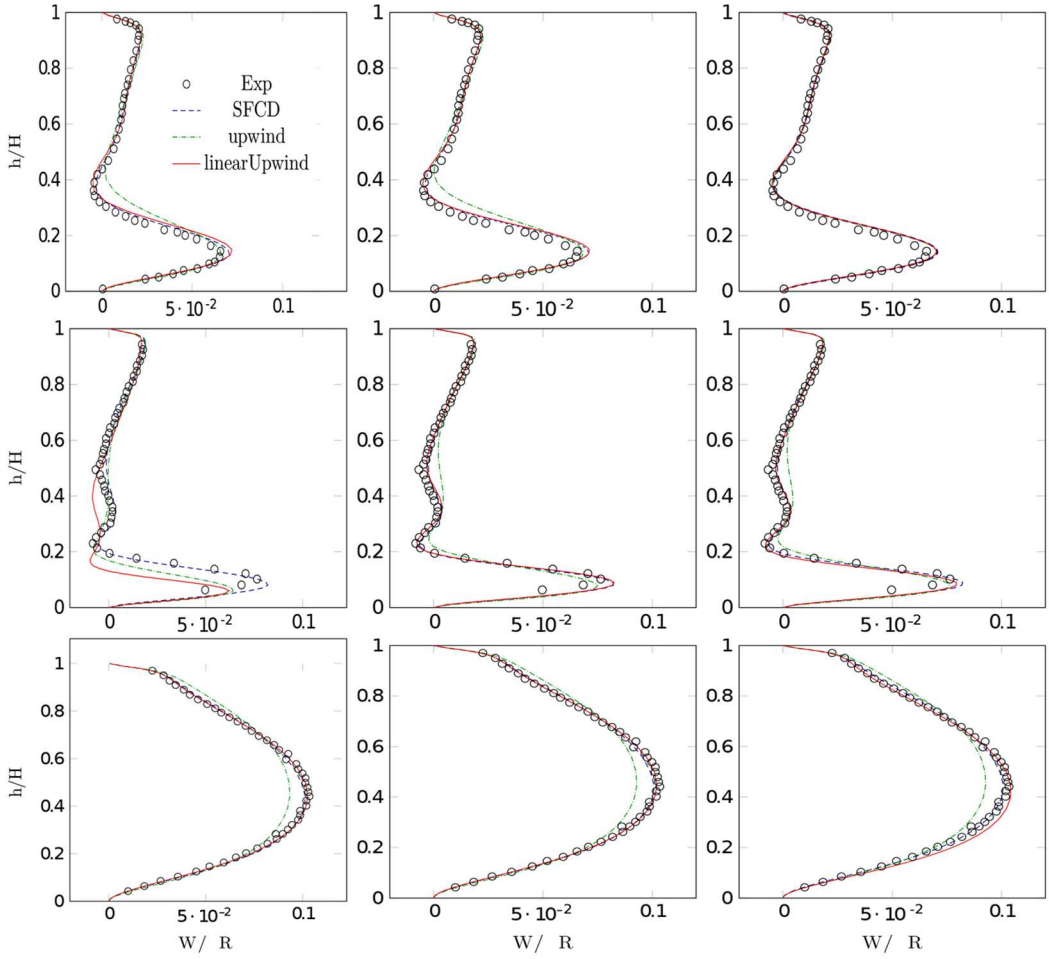

Figure 4. Axial velocity along the centerline. (From top to bottom: case A, case B, and case C. From left to right: coarse, medium, and fine grid.)

Table 2. Upwind Scheme

case	Ar	*Re*	grid size	max velocity	error (%)	vortex breakdowns
Exp1	2.5	1010	–	0.103385	–	non
A1	2.5	1010	1320	0.092695	10.3	non
A2	2.5	1010	2352	0.092827	10.21	non
A3	2.5	1010	4176	0.093279	9.78	non
Exp2	1.5	1290	–	0.065676	–	1
B1	1.5	1290	2204	0.070203	6.89	non
B2	1.5	1290	2640	0.068319	4.02	non
B3	1.5	1290	5104	0.065987	0.47	non
Exp3	2.5	2200	–	0.076415	–	2
C1	2.5	2200	2352	0.064115	16.096	non
C2	2.5	2200	4640	0.074994	1.8595	non
C3	2.5	2200	7800	0.076175	0.3140	non

Table 3. SFCD Scheme

case	Ar	*Re*	grid size	max velocity	error (%)	vortex breakdowns
Exp1	2.5	1010	–	0.103385	–	non
A1	2.5	1010	1320	0.1012	2.54	non
A2	2.5	1010	2352	0.10076	2.51	non
A3	2.5	1010	4176	0.10079	2.11	non
Exp2	1.5	1290	–	0.065676	–	1
B1	1.5	1290	2204	0.070737	7.71	1
B2	1.5	1290	2640	0.070666	7.60	1
B3	1.5	1290	5104	0.070635	7.55	1
Exp3	2.5	2200	–	0.076415	–	2
C1	2.5	2200	2352	0.082251	7.64	2
C2	2.5	2200	4640	0.082196	7.57	2
C3	2.5	2200	7800	0.081964	7.26	2

computed mean axial and tangential velocity profiles identify the input parameters at the flow inlet.

The swirl number S (eq 26) represents the ratio of the axial flux of the tangential momentum to the axial flux of the axial momentum multiplied by the radius,

$$S = \frac{1}{R}\frac{\int_0^R \upsilon_t \upsilon_z r^2 \, \mathrm{d}r}{\int_0^R \upsilon_z{}^2 r \, \mathrm{d}_r} \tag{26}$$

For the swirling case, the swirl number is ∼0.6, based on the inlet radius (R = $D/2$); υ_t and υ_z indicate the time-averaged tangential and axial velocities, respectively. Figure 7 shows the applied velocity profiles at the inlet for the swirling case (S = 0.6).

The transient PisoFOAM solver is employed to handle the pressure−velocity coupling. For the temporal differentiation, the second-order backward scheme is applied. All simulations were run with a constant time step of (2×10^{-4}). The minimum required time step was calculated using the Courant−Friedrichs-Lewy (CFL) stability condition. The considered EVMs were

https://doi.org/10.1021/acs.iecr.1c00158
Ind. Eng. Chem. Res. 2021, 60, 6016−6026

Table 4. Linear-Upwind Scheme

case	Ar	*Re*	grid size	max velocity	error (%)	vortex breakdowns
Exp1	2.5	1010	–	0.103385	–	non
A1	2.5	1010	1320	0.10196	1.38	non
A2	2.5	1010	2352	0.10251	0.846	non
A3	2.5	1010	4176	0.10416	0.75	non
Exp2	1.5	1290	–	0.065676	–	1
B1	1.5	1290	2204	0.071912	9.50	1
B2	1.5	1290	2640	0.071178	8.38	1
B3	1.5	1290	5104	0.07086	7.89	1
Exp3	2.5	2200	–	0.076415	–	2
C1	2.5	2200	2352	0.062078	18.76	2
C2	2.5	2200	4640	0.082545	8.02	2
C3	2.5	2200	7800	0.079308	3.79	2

evaluated for the final mesh size, which was obtained after performing grid independence tests. The characteristic final mesh size was fixed and kept constant for all comparison studies. The time step was adjusted in order not to exceed the maximum Courant number of 1 for any considered simulations. The equations residuals were set to fall below a predetermined residual tolerance value over a successive number of iterations. For the pressure equation, the residual value was 10^{-8}, whereas, for all other variables, a value of 10^{-6} was considered to be sufficient. Characteristic profiles representing primitive variables values were also monitored, to ensure that these are converged.

RESULTS AND DISCUSSION

The first case study is the no-swirling flow at $S = 0$. Figure 8 compares the axial velocity contours predicted by the standard $k-\epsilon$, RNG $k-\epsilon$, and the SST $k-\omega$ models with the new SSTCCM model.

It can be seen that the standard $k-\epsilon$ model predicts a very weak recirculation zone, with a percentage error of 63.9% in predicting the reattachment position, compared to the experimental value ($X_r/h = 9.3$). This could be attributed to the isotropic nature of this model. The RNG $k-\epsilon$ model performs better than the former, generating 39.3% error, but still not as required. The congruence between the results of both the SST $k-\omega$ and SSTCCM models and the experimental data was manifested by a smaller percentage error of 25.8%. Figure 9 shows that the SSTCCM model performs well, with regard to predicting axial mean velocity profiles along the longitudinal axis when validating it against the experimental results of Dellenback et al.[21]

At a moderate to a high level of swirling strengths, the flow field starts exhibiting an indistinct and complex phenomenon of an unsteady asymmetry that is usually observed in swirling flows.

Table 5. Geometric Parameters for the Sudden Expansion Case

parameter	dimension (m)
inlet diameter, D	0.05078
inlet length, L	$2D$
outer diameter, D_2	$1.94D$
outer length, L_2	$10D$
expansion ratio, D_2/D	1.94

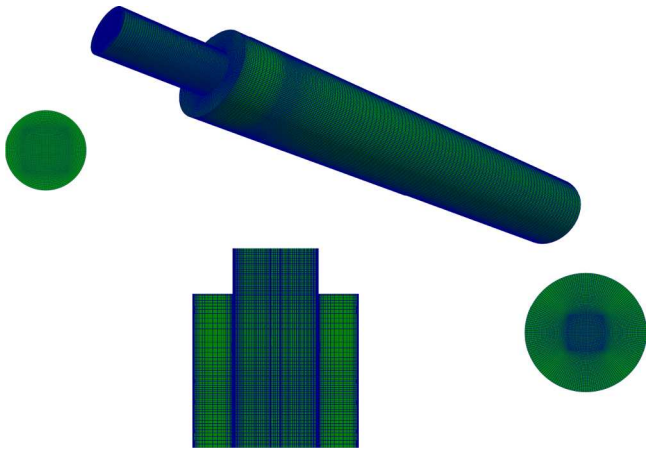

Figure 6. Computational domain for the sudden expansion geometry.

This feature is initiated with the on-axis recirculation and the vortex breakdown phenomenon.

Figures 10 and 11 show the extent of the recirculation zone at ($S = 0.6$) through contours of axial velocity and static pressure. As the swirling level increases to moderate values, the flow has a tendency toward asymmetrical form with central recirculation, signaling the start of vortex breakdown. This is due to the viscous dissipation of the tangential velocity component, which produces an adverse pressure gradient on the centerline of the tube.

Figure 12 reassures that the SSTCCM model performs well with regard to predicting axial and tangential mean velocity profiles along the longitudinal axis, when validating it against the experimental results of Dellenback et al.[21]

There is a significant challenge in precisely predicting the unsteady characteristics of the swirling flow with vortex breakdown utilizing the conventional EVMs. This weakness is clearly observed in Figure 10, where the standard $k-\epsilon$, RNG $k-\epsilon$, and the SST $k-\omega$ models were unable to capture the vortex breakdown phenomenon. The SSTCCM model is better-suited to capture the location and extent of the central recirculation zone in the swirling flow immediately after expansion.

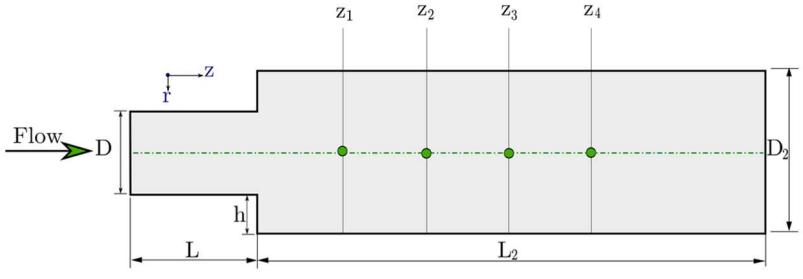

Figure 5. Schematic diagram of the sudden expansion geometry.

https://doi.org/10.1021/acs.iecr.1c00158
Ind. Eng. Chem. Res. 2021, 60, 6016−6026

Table 6. Setup of the Sudden Expansion Geometry Boundary Conditions

boundary	U (m/s)	p (m^2/s^2)	k (m^2/s^2)	ϵ (m^2/s^3)	ω (1/s)
inlet	(0 0 0.473)	zero gradient	$\frac{3}{2}(I \times U)^2$	$\frac{k^{3/2}}{I \times Ri}$	$\frac{k^{1/2}}{C_\mu \times I \times Ri}$
outlet	zero gradient	fixed value (0)	zero gradient	zero gradient	zero gradient
walls	fixed (0 0 0)	zero gradient	kqR wall function	ϵ wall function	ω wall function

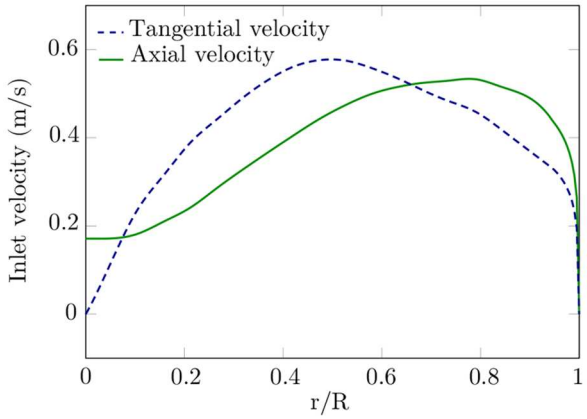

Figure 7. Inlet velocity profiles of the computational domain for the swirl case at $S = 0.6$.

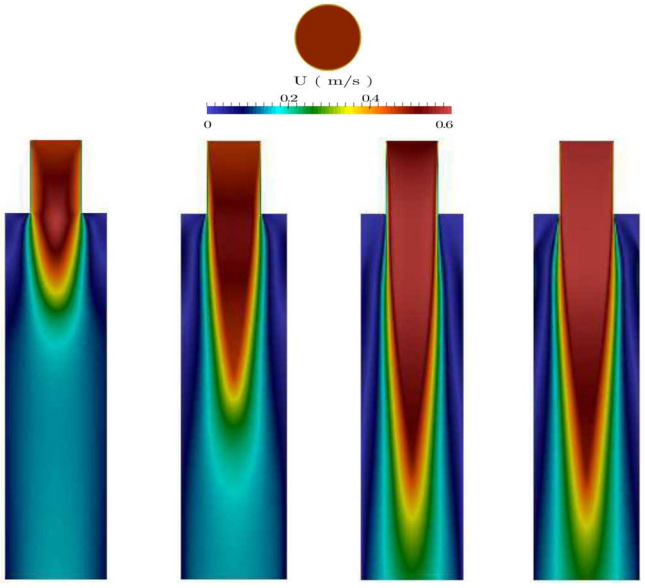

Figure 8. Contour plots of axial velocity for no-swirling case ($S = 0$) flow through the sudden expansion 3D pipe. From left to right: $k-\epsilon$, RNG $k-\epsilon$, SST $k-\omega$, and SSTCCM.

Figure 13 presents the slices in the z-plane of the swirling flow case at ($S = 0.6$) visualized by instantaneous velocity magnitude contours from the inlet to the outlet, which clearly show the unsteadiness and vortex breakdown phenomenon. This contrasts with Figure 14 at $S = 0$ for the nonswirling flow case, where the flow is developing uniformly without showing any vortex breakdown.

About 11 h of computation time were required for the simulation with the standard $k-\epsilon$ model. The RNG $k-\epsilon$ model simulations consumed 13.5 h, the SST $k-\omega$ took 21 h, and the SSTCCM simulations required 23.5 h. All simulation were performed on four 2.50 GHz Intel i5−3200 M processors.

The Reynolds Stress Model (RSM) could be treated as an alternative approach for the simulations presented in this study. The model accounts for anisotropic Reynolds stresses in the flow, contrary to the EVMs models, which do not provide the directional dependence of the turbulent stresses. The model explicitly accounts for the effects of streamline curvature and rotation. Although the RSM approach is superior to any EVM approaches and has been successfully used for computing swirling flows[26,27] (for example, to resolve secondary flows in gas vortex units),[28] it has been found that the model is incapable of resolving all of the deficiencies of the two-equation models for simulating turbulent swirling flows. Tsai et al.[29] compared the RSM simulations with measurements and reported that, for weakly swirling flows ($S = 0.3$), the strength of the decay of swirl-induced deceleration of the axial velocity is not reproduced correctly. Lu and Semiao[30] reported that, for this flow regime, the RSM model does not resolve the intensity of turbulence along the center line correctly. The RSM model also carries significant computations overhead, because the additional equations for the Reynolds stresses must be solved in three dimensions and, therefore, the model was not considered in the present study. On the other hand, the common deficiency of the closure model modifications is related to the fact that a scalar formula does not distinguish directional components of the covariance tensor of Reynolds stresses. To elevate this problem, various other modifications of a closure model have been applied. The turbulent production limiters meant to avoid excessive turbulent kinetic energy prediction in stagnation regions were proposed by Menter[8] and by Kato and Launder.[31] The production limiters replace the quadratic strain contribution with the strain rate multiplied by the vorticity rate. In other methods, the original Kato−Launder approach was replaced with a linear combination of the unmodified production term and the Kato−Launder modified production term. Reboud et al.[32] have proposed the introduction of a production limiting term, which is a simple arbitrary multiplier acting on the turbulence viscosity term.

CONCLUSIONS

The numerical simulation have been performed using the developed shear stress transport model with curvature correction modification. The results were compared with other popular turbulence closure models in flow regimes that are subject to directional forces, such as those due to system rotation. The model was successfully validated against experimental data representing the flow in a confined cylinder with a rotating lid and the 3D swirling flow through a sudden expansion pipe. The model that was designed for practical simulations of complex cases requiring a quick turnaround time to complete calculations proved to reproduce the flow profiles with better accuracy than the conventional EVMs. The proposed approach allowed capturing the location of the vortex breakdown phenomenon in the swirling flow.

https://doi.org/10.1021/acs.iecr.1c00158
Ind. Eng. Chem. Res. 2021, 60, 6016−6026

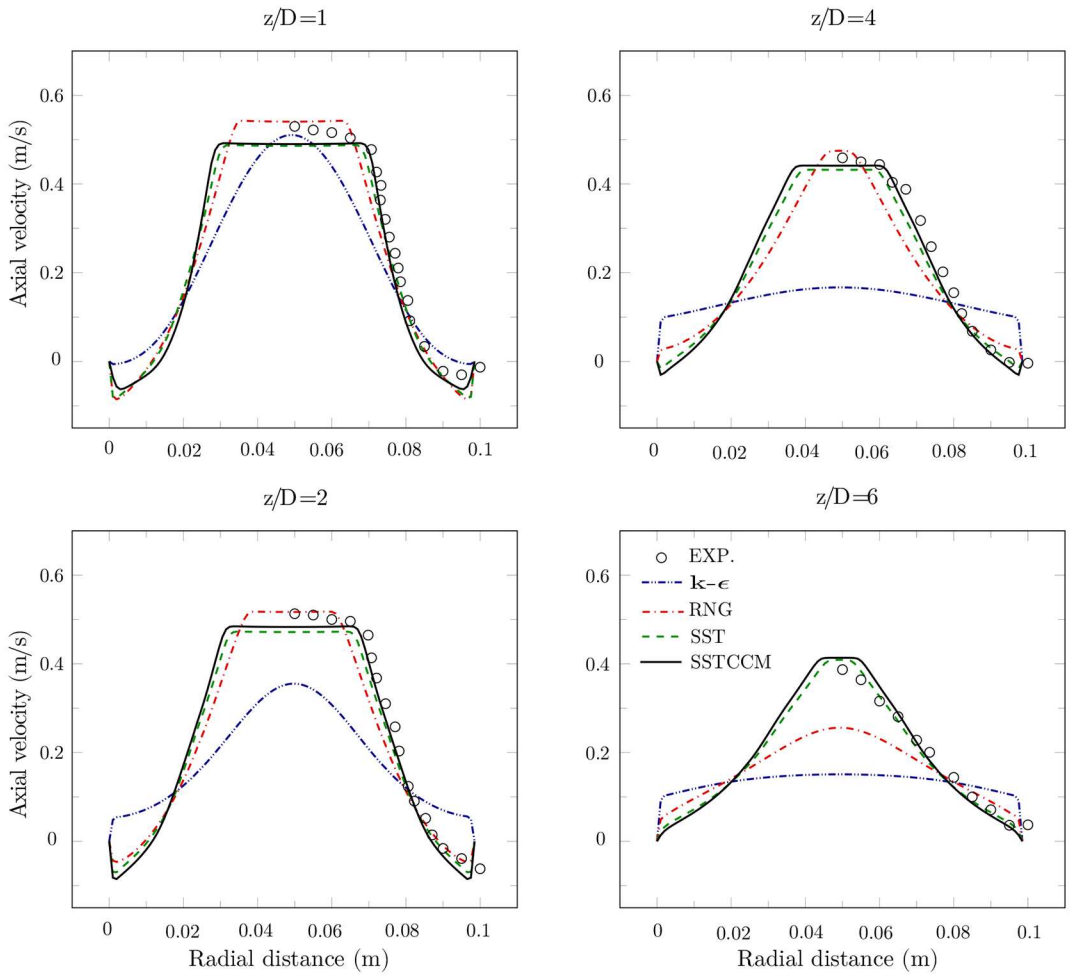

Figure 9. Axial mean velocity profiles upstream the sudden expansion pipe, no-swirling flow case ($S = 0$); comparison between the $k-\epsilon$, RNG, SST, SSTCCM, and the LDA measurements. [Experimental results reprinted in part with permission from ref 21. Copyright 1988, AIAA.]

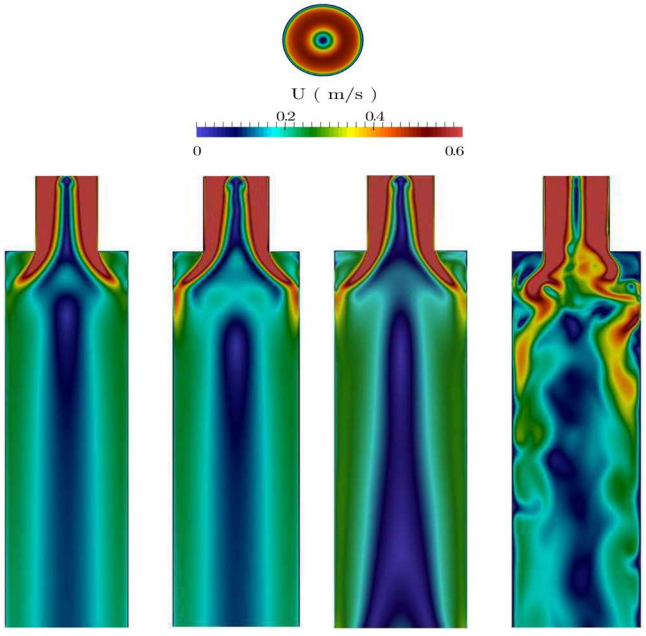

Figure 10. Contours of axial velocity for $S = 0.6$ swirling flow through the sudden expansion 3D pipe. From left to right:$S = 0.6$ $k-\epsilon$, RNG $k-\epsilon$, SST $k-\omega$, and SSTCCM.

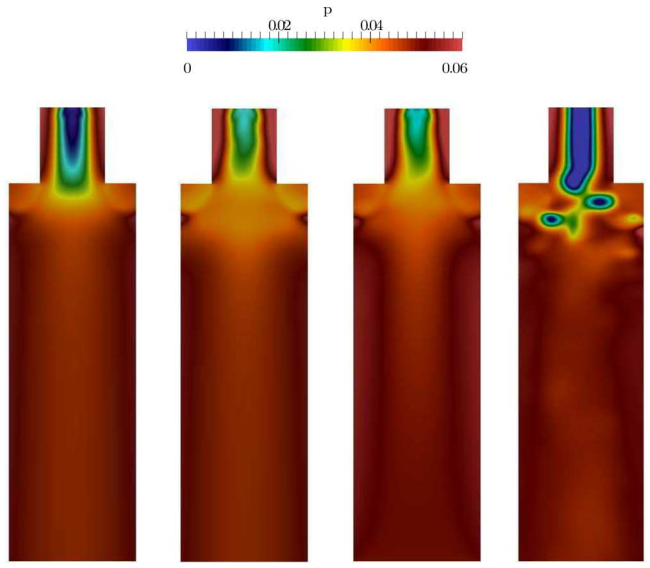

Figure 11. Contours of static pressure [m^2/s^2] for $S = 0.6$ swirling flow through the sudden expansion 3D pipe. From left to right: $k-\epsilon$, RNG $k-\epsilon$, SST $k-\omega$, and SSTCCM.

https://doi.org/10.1021/acs.iecr.1c00158
Ind. Eng. Chem. Res. 2021, 60, 6016−6026

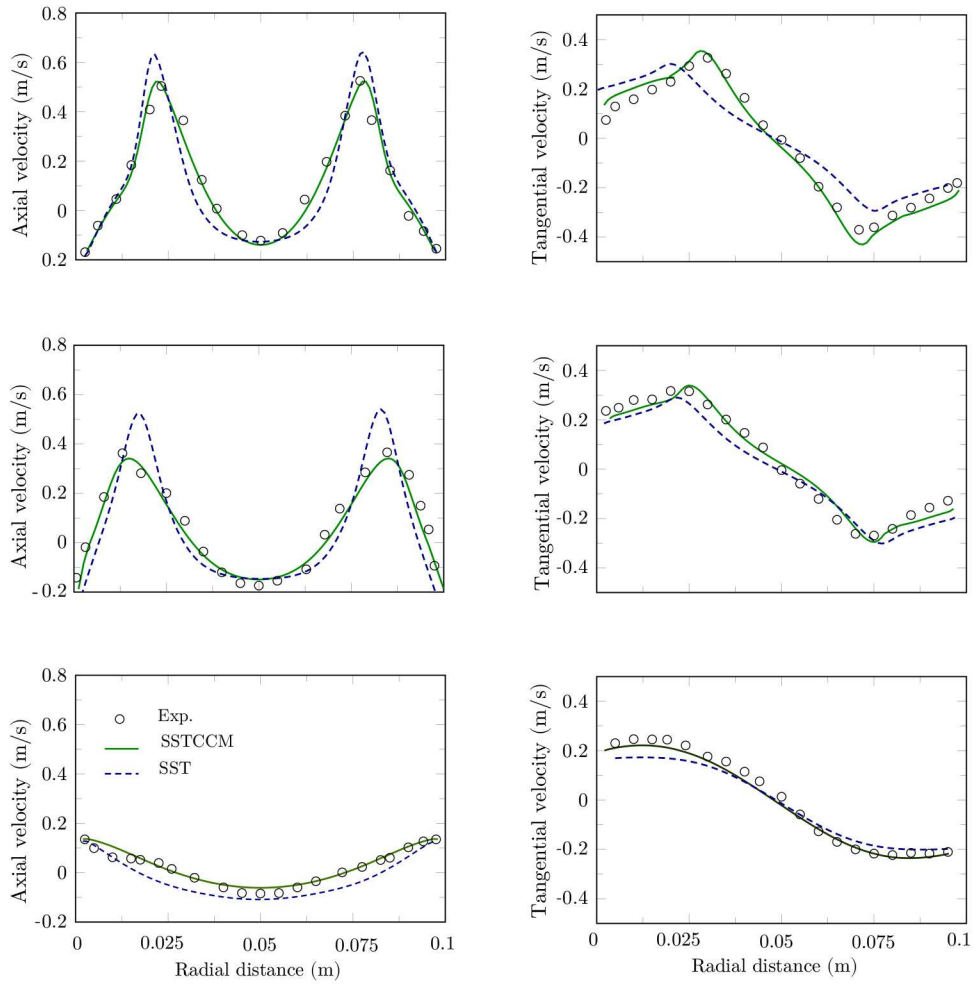

Figure 12. Mean axial (left) and tangential (right) velocity profiles upstream the sudden expansion pipe for ($S = 0.6$) swirling flow case at $z/D = 0.5$, 1, and 3; comparison between the SST model with and without rotation corrections and the LDA measurements. [Experimental results reprinted in part with permission from ref 21. Copyright 1988, AIAA.]

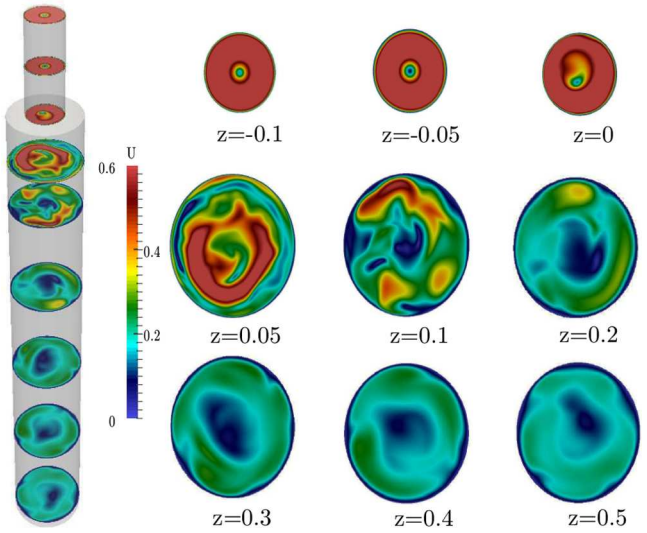

Figure 13. Slices in the z-plane of the swirling flow visualized by instantaneous velocity magnitude contours from the inlet to the outlet at $Re = 30\,000$ and $S = 0.6$, using SSTCCM.

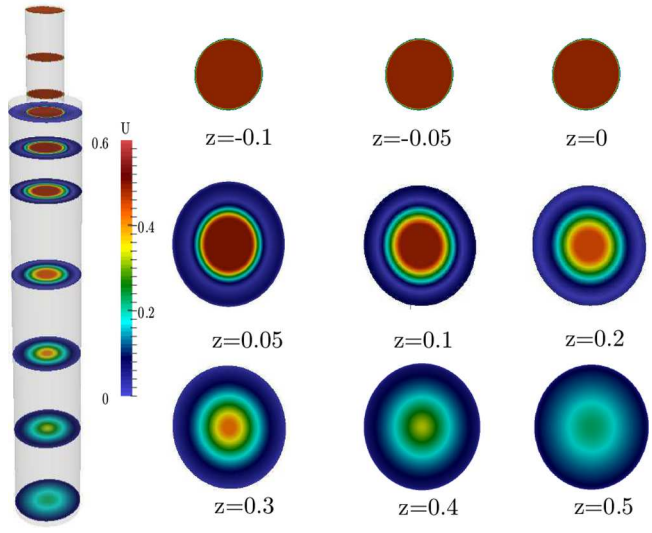

Figure 14. Slices in the z-plane of the no-swirling flow visualized by instantaneous velocity magnitude contours from the inlet to the outlet at $Re = 30\,000$ and $S = 0$, using SSTCCM.

https://doi.org/10.1021/acs.iecr.1c00158
Ind. Eng. Chem. Res. 2021, 60, 6016−6026

■ ASSOCIATED CONTENT

Supporting Information

The Supporting Information is available free of charge at https://pubs.acs.org/doi/10.1021/acs.iecr.1c00158.

(ZIP)

Special Issue Paper

Originally intended for the special issue Characterization and Applications of Fluidic Devices without Moving Parts, *Ind. Eng. Chem. Res.* **2020**, Volume 59, Issue 9.

■ AUTHOR INFORMATION

Corresponding Author

Andrzej F. Nowakowski − *Sheffield Fluid Mechanics Group, Department of Mechanical Engineering, The University of Sheffield, Sheffield S1 3JD, United Kingdom;* orcid.org/0000-0002-5018-2661; Phone: +44(0)1142227812; Email: a.f.nowakowski@sheffield.ac.uk

Authors

Yaser H. Alahmadi − *Mechanical Engineering Department, Islamic University of Madinah, Madinah 42351, Saudi Arabia*

Sawsan A. Awadh − *Sheffield Fluid Mechanics Group, Department of Mechanical Engineering, The University of Sheffield, Sheffield S1 3JD, United Kingdom; Department of Mechanical Engineering, The University of Babylon, Babylon, Iraq*

Complete contact information is available at: https://pubs.acs.org/10.1021/acs.iecr.1c00158

Notes

The authors declare no competing financial interest.

■ ACKNOWLEDGMENTS

This work was funded by the Iraqi Ministry of Higher Education and Scientific Research, under Award No. PO/34/20264 for the Ph.D. scholarship program. Computational resources were provided by the HPC High Performance Computing Service at the University of Sheffield.

■ REFERENCES

(1) Howard, J.; Patankar, S.; Bordynuik, R. Flow prediction in rotating ducts using Coriolis-modified turbulence models. *J. Fluids Eng.* **1980**, *102*, 456−461.

(2) Gooray, A.; Watkins, C.; Aung, W. Improvements to the *k*-Epsilon Model for Calculations of Turbulent Recirculating Flow. In *4th Symposium on Turbulent Shear Flows*; 1984; p 18.

(3) Park, S.; Chung, M. Curvature-dependent two-equation model for prediction of turbulent recirculating flows. *AIAA J.* **1989**, *27*, 340−344.

(4) Spalart, P.; Shur, M. On the sensitization of turbulence models to rotation and curvature. *Aerosp. Sci. Technol.* **1997**, *1*, 297−302.

(5) Knight, D.; Saffman, P. Turbulence model predictions for flows with significant mean streamline curvature. *AIAA J.* **1978**, *258*, 1978.

(6) Smirnov, P. E.; Menter, F. R. Sensitization of the SST turbulence model to rotation and curvature by applying the Spalart−Shur correction term. *J. Turbomach.* **2009**, *131*, 041010.

(7) Alahmadi, Y. H.; Nowakowski, A. F. Modified shear stress transport model with curvature correction for the prediction of swirling flow in a cyclone separator. *Chem. Eng. Sci.* **2016**, *147*, 150−165.

(8) Menter, F. R. Two-equation eddy-viscosity turbulence models for engineering applications. *AIAA J.* **1994**, *32*, 1598−1605.

(9) Shur, M. L.; Strelets, M. K.; Travin, A. K.; Spalart, P. R. Turbulence modeling in rotating and curved channels: Assessing the Spalart-Shur correction. *AIAA J.* **2000**, *38*, 784−792.

(10) Hellsten, A. Some improvements in Menter's k-ω SST turbulence model. *AIAA J.* **1998**, AIAA-98-2554.

(11) Chen, G.; Xiong, Q.; Morris, P. J.; Paterson, E. G.; Sergeev, A.; Wang, Y. OpenFOAM for computational fluid dynamics. *Not. AMS* **2014**, *61*, 354−363.

(12) Fujimura, K.; Yoshizawa, H.; Iwatsu, R.; Koyama, H. S.; Hyun, J. M. Velocity measurements of vortex breakdown in an enclosed cylinder. *J. Fluids Eng.* **2001**, *123*, 604−611.

(13) Escudier, M. Observations of the flow produced in a cylindrical container by a rotating endwall. *Exp. Fluids* **1984**, *2*, 189−196.

(14) Simpson, A.; Ranade, V. V. Flow characteristics of vortex based cavitation devices. *AIChE J.* **2019**, *65*, No. e16675.

(15) Nowakowski, A. F.; Doby, M. J. The numerical modelling of the flow in hydrocyclones. *KONA* **2008**, *26*, 66−80.

(16) Banerjee, C.; Chaudhury, K.; Majumder, A. K.; Chakraborty, S. Swirling flow hydrodynamics in hydrocyclone. *Ind. Eng. Chem. Res.* **2015**, *54*, 522−528.

(17) Ghodrat, M.; Kuang, S. B.; Yu, A. B.; Vince, A.; Barnett, G. D.; Barnett, P. J. Computational study of the multiphase flow and performance of hydrocyclones: effects of cyclone size and spigot diameter. *Ind. Eng. Chem. Res.* **2013**, *52*, 16019−16031.

(18) Parvaz, F.; Hosseini, S. H.; Elsayed, K.; Ahmadi, G. Numerical investigation of effects of inner cone on flow field, performance and erosion rate of cyclone separators. *Sep. Purif. Technol.* **2018**, *201*, 223−237.

(19) Yang, X.; He, Z.; Dong, S.; Tan, H. Combustion characteristics of bluff-body turbulent swirling flames with coaxial air microjet. *Energy Fuels* **2017**, *31*, 14306−14319.

(20) Hernandez, B.; Fraser, B.; Martin de Juan, L.; Martin, M. Computational Fluid Dynamics (CFD) modeling of swirling flows in Industrial counter-current spray-drying towers under fouling conditions. *Ind. Eng. Chem. Res.* **2018**, *57*, 11988−12002.

(21) Dellenback, P.; Metzger, D.; Neitzel, G. Measurements in turbulent swirling flow through an abrupt axisymmetric expansion. *AIAA J.* **1988**, *26*, 669−681.

(22) Wang, P.; Bai, X.-S.; Wessman, M.; Klingmann, J. Large eddy simulation and experimental studies of a confined turbulent swirling flow. *Phys. Fluids* **2004**, *16*, 3306−3324.

(23) Gyllenram, W.; Nilsson, H.; Davidson, L. On the failure of the quasicylindrical approximation and the connection to vortex breakdown in turbulent swirling flow. *Phys. Fluids* **2007**, *19*, 045108.

(24) Javadi, A.; Nilsson, H. A comparative study of scale-adaptive and large-eddy simulations of highly swirling turbulent flow through an abrupt expansion. *IOP Conference Series: Earth and Environmental Science* **2014**, *22*, 022017.

(25) Paik, J.; Sotiropoulos, F. Numerical simulation of strongly swirling turbulent flows through an abrupt expansion. *Int. J. Heat Fluid Flow* **2010**, *31*, 390−400.

(26) Leschziner, M. A.; Hogg, S. Computation of highly swirling confined flow with a Reynolds stress turbulence model. *AIAA J.* **1989**, *27*, 57−63.

(27) Pandare, A.; Ranade, V. V. Flow in vortex diodes. *Chem. Eng. Res. Des.* **2015**, *102*, 274−285.

(28) Niyogi, K.; Torregrosa, M. M.; Marin, G. B.; Heynderickx, G. J.; Shtern, V. N. On the mechanisms of secondary flows in a gas vortex unit. *AIChE J.* **2018**, *64*, 1859−1873.

(29) Tsai, J. H.; Lin, C. A.; Lu, C. M. Modelling dump combustor flows with and without swirl at the inlet using Reynolds stress models. *Int. J. Numer. Methods Heat Fluid Flow* **1995**, *5*, 577−588.

(30) Lu, P.; Semiao, V. A new second-moment closure approach for turbulent swirling confined flows. *Int. J. Numer. Methods Fluids* **2003**, *41*, 133−150.

(31) Kato, M.; Launder, B. The modelling of turbulent flow around stationary and vibrating square cylinders. In *9th Symposium on Turbulent Shear Flows*, 1993.

(32) Reboud, J.-L.; Stutz, B.; Coutier, O. Two Phase Flow Structure of Cavitation: Experiment and Modeling of Unsteady Effects. In *3rd International Symposium on Cavitation (CAV1998)*, Grenoble, France, 1998.